Supplementary Materials for

Solvent polarizability governs Li^+ transport kinetics for high energy lithium metal batteries

Chuangchao Sun[1+*], Linxiang Chen[1+], Junyi Hua[2+], Shengpeng Zhang[1], Yong Li[3], Liyi Zhao[4], Hao Cheng[5], Daixin Ye[6*], Haikuo Zhang[2*], Lianbang Wang[1*], Xiulin Fan[2*]

[1]State Key Laboratory of Green Chemical Synthesis and Conversion, College of Chemical Engineering, Zhejiang University of Technology, Hangzhou 310014, China.

[2]State Key Laboratory of Silicon and Advanced Semiconductor Materials, School of Materials Science and Engineering, Zhejiang University, Hangzhou 310027, China.

[3]State Key Laboratory of Space Power-Sources Technology, Shanghai Institute of Space Power-Sources, Shanghai 200245, China.

[4]i-Lab, Suzhou Institute of Nano-Tech and Nano-Bionics, Chinese Academy of Science, Suzhou 215123, China.

[5]Zhejiang Key Laboratory of Intelligent Manufacturing for Functional Chemicals, ZJU-Hangzhou Global Scientific and Technological Innovation Center, Zhejiang University, Hangzhou 311215, China.

[6]Department of Chemistry & Institute for Sustainable Energy, College of Sciences, Shanghai University, Shanghai 200444, China.

[+]These authors contributed equally: Chuangchao Sun, Linxiang Chen, Junyi Hua.

*Corresponding authors. E-mail: suncc@zjut.edu.cn, daixinye@shu.edu.cn, zhanghaikuo@zju.edu.cn, Wanglb99@zjut.edu.cn, xlfan@zju.edu.cn.

Supplementary Note 1

Polarizability (α) is a fundamental molecular property that quantifies the ease with which the electron cloud of a molecule can be distorted under an external electric field. It describes the proportional relationship between the induced dipole moment (P_{ind}) and the applied electric field (E) according to the classical linear polarization expression: $\boldsymbol{P_{ind} = \alpha E}$[1,2]. A higher polarizability implies that the molecule exhibits a stronger electronic response to the electric field, leading to a larger induced dipole moment and a higher degree of electronic redistribution. In contrast, a lower polarizability indicates a more rigid electronic structure that resists deformation by the field. In the context of electrolyte systems for lithium metal batteries, polarizability serves as a quantitative descriptor for evaluating how inert solvents respond to interfacial electric fields. Unlike parameters such as dipole moment or dielectric constant, which mainly reflect the static polarity of a molecule, polarizability captures its dynamic polarization capability—that is, how its instantaneous electronic configuration adapts to an external perturbation. This property becomes particularly relevant at the electrode/electrolyte interface, where the local electric field can reach magnitudes of 10^7–10^8 V/m. Under such intense fields, solvents with higher polarizability tend to generate larger induced dipoles, which can strengthen ion–dipole interactions and disturb the coordination between anions and Li^+. Conversely, solvents with low polarizability produce minimal electronic deformation, thereby preserving the original anion-rich solvation structure and maintaining interfacial stability. Therefore, polarizability provides a physically grounded parameter for describing the electric-field sensitivity of inert solvents and rationalizing their

impact on interfacial Li^+ kinetics.

Supplementary Note 2

To experimentally quantify the polarizability of inert solvents, we employed an electrochemical polarization method based on dielectric response measurements in an ideal parallel-plate capacitor configuration[3]. The polarization response of inert solvents was experimentally evaluated using a symmetric parallel-plate cell, where two stainless-steel electrodes were separated by a Celgard 2325 membrane serving as the spacer and physical separator. Approximately 100 μL of pure solvent was injected into the cell to ensure complete wetting and filling of the inter-electrode space. To eliminate the influence of ionic conduction, no lithium salts or other ionic species were added, and only the pure inert solvent was used as the dielectric medium. Electrochemical impedance spectroscopy (EIS) measurements were carried out using a precision impedance analyzer (e.g. lvium electrochemical workstation) over a frequency range of 1 kHz to 1 MHz, under a small sinusoidal perturbation amplitude of 10 mV. The measurements were conducted at a controlled temperature of 25 ± 0.5 °C. The resulting impedance spectra were fitted using an equivalent circuit model consisting of a parallel capacitor and a leakage resistor, which accounts for the dielectric polarization and residual conduction components, respectively.

The real and imaginary components of the complex impedance (Z', Z'') were converted into capacitance (C) and phase angle (θ) through standard relations[4]:

$$C=\frac{-1}{2\pi fZ''}sin(-\theta)$$

At low frequencies, the system exhibits negligible capacitive response due to the absence of mobile ions. In the high-frequency region, the dielectric relaxation of the

solvent dominates, characterized by a phase angle approaching −90°, confirming that dipolar polarization governs the response behavior. The ideal capacitance C_{id} at high frequencies was extracted and normalized by the geometric parameters of the cell to calculate the relative permittivity ε_r. The molecular polarizability (α) was then estimated using the Clausius–Mossotti relation[5]:

$$\frac{3\varepsilon_r - 1}{\varepsilon_r + 2} = \frac{N\alpha}{3\varepsilon_0}$$

where N is the molecular number density of the solvent. The calculated α values for different inert solvents are summarized in Supplementary Table 1. Due to the limited experimental precision and the influence of interfacial effects, the obtained polarizability values represent only relative magnitudes among different inert solvents. The absolute polarizability values should refer to those calculated from density functional theory (DFT) for quantitative comparison.

Supplementary Note 3

(1) The setting of the vertical electron affinity (VEA)

The vertical electron affinity (VEA) of a solvent is a key parameter for its compatibility with the lithium metal negative electrode[6]. A more negative VEA indicates better cathodic stability, as it suggests that the solvent is less likely to undergo reduction during Li plating/stripping cycles. To prevent solvent reduction from interfering with lithium metal deposition, a threshold for VEA was set during the screening process, ensuring both stable Li plating/stripping and accurate evaluation of the electrochemical performance.

(2) The setting of the vertical ionization potential (VIP)

The vertical ionization potential (VIP) is an important indicator for assessing the solvent's compatibility with the positive electrode during the lithium-ion battery's operation[7]. A higher VIP signifies that the solvent is more resistant to oxidation, which is vital for maintaining the stability of the solvent when exposed to the high voltage environments of the positive electrode during charge cycles. However, excessively high VIP values can increase the risk of reduced ionic conductivity or sluggish charge transfer. Therefore, solvents were selected based on their VIP, with an optimal range that balances oxidation resistance at the positive electrode while maintaining electrolyte performance.

Supplementary Note 4

To quantitatively evaluate the desolvation energy difference among various electrolytes, we employed an H-type electrochemical cell configuration, which allows for direct comparison of the chemical potential of Li^+ in different electrolyte systems without electron exchange between the two half-cells. The H-type cell consists of two identical compartments connected by a glass bridge containing four layers of Celgard 2325 separators, which serve as an ionic pathway while effectively preventing electronic conduction. Each compartment was filled with a different test electrolyte (ca. 20 mL), and a high-purity lithium metal foil was immersed into each side to act as both the working and counter electrodes. During the dissolution of lithium into the electrolytes, a potential difference spontaneously arises due to the variation in Li^+ solvation thermodynamics. This open-circuit potential (ΔE) reflects the relative free-energy difference between the solvated Li^+ species in the two electrolytes, which can be expressed as[8]:

$$\Delta G_{\text{desolv}} = -nF\Delta E$$

where ΔG_{desolv} represents the desolvation free-energy difference, n is the number of electrons transferred per Li^+ ion ($n = 1$), and F is the Faraday constant. A larger potential difference corresponds to a higher energy barrier for Li^+ desolvation in the corresponding electrolyte. The measured potential difference was recorded after the system reached equilibrium (typically within 10 min), and the results were averaged over three independent measurements for each electrolyte pair to ensure reproducibility. The obtained ΔE values were further correlated with the inert solvent polarizability

parameter (α) to reveal a near-linear dependence (Fig. 2e), confirming that solvents with higher polarizability induce larger desolvation energies. It is worth noting that due to the limited precision of the experimental setup and the presence of residual concentration polarization, the absolute values of the measured potentials represent relative desolvation energies. Therefore, the absolute magnitudes should be interpreted in conjunction with the calculated desolvation energies derived from DFT simulations for consistency and accuracy.

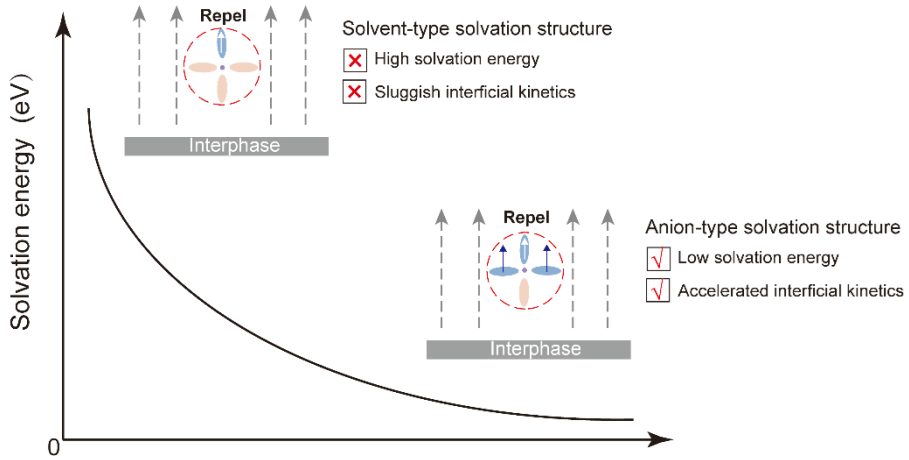

Supplementary Fig. 1 | Schematic illustration of desolvation energy at interfaces with different solvation structures.

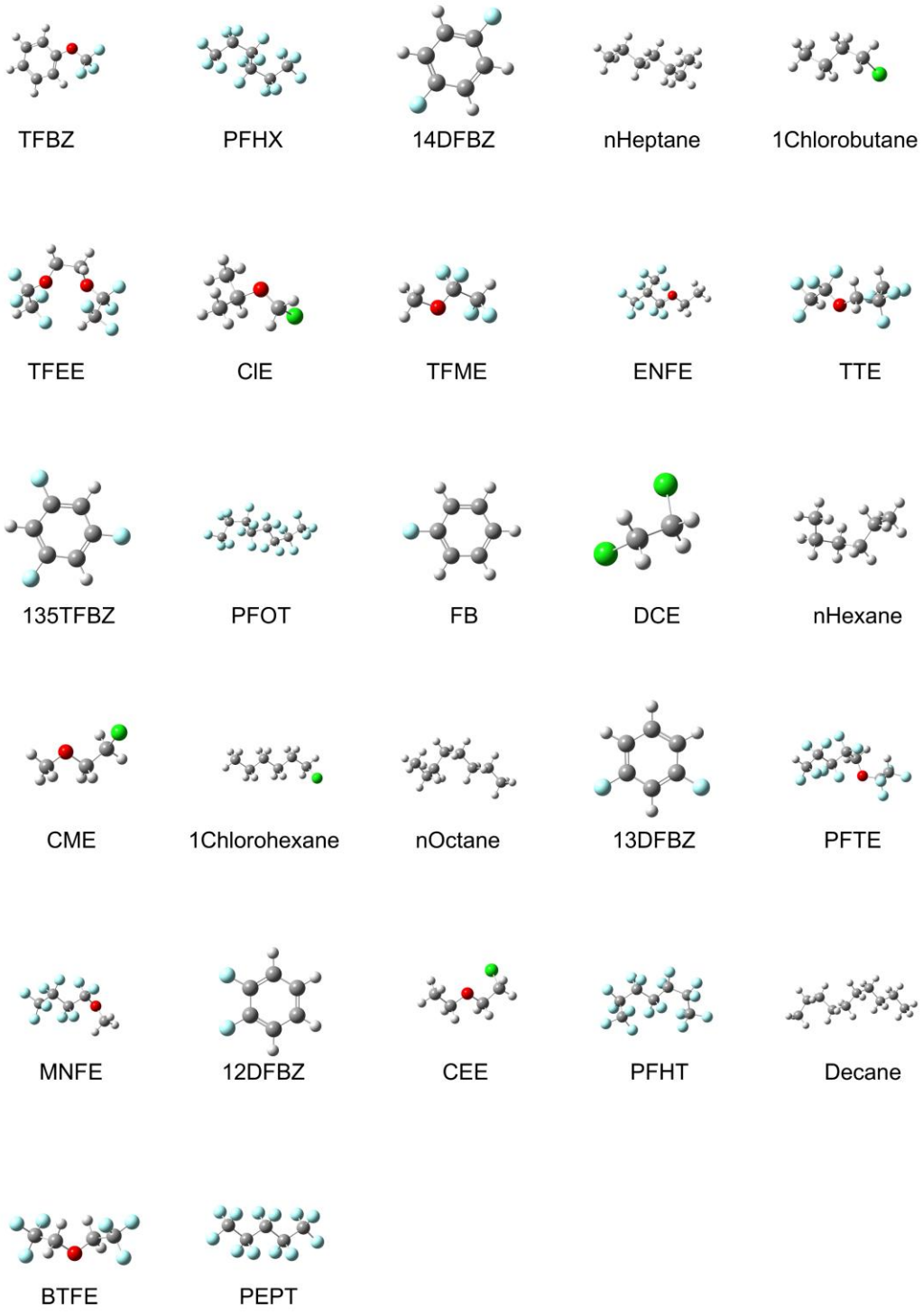

Supplementary Fig. 2 | Molecular structures of the inert solvents. The coloured spheres represent different atom types: C (black), F (blue), H (grey), O (red), and Cl (green).

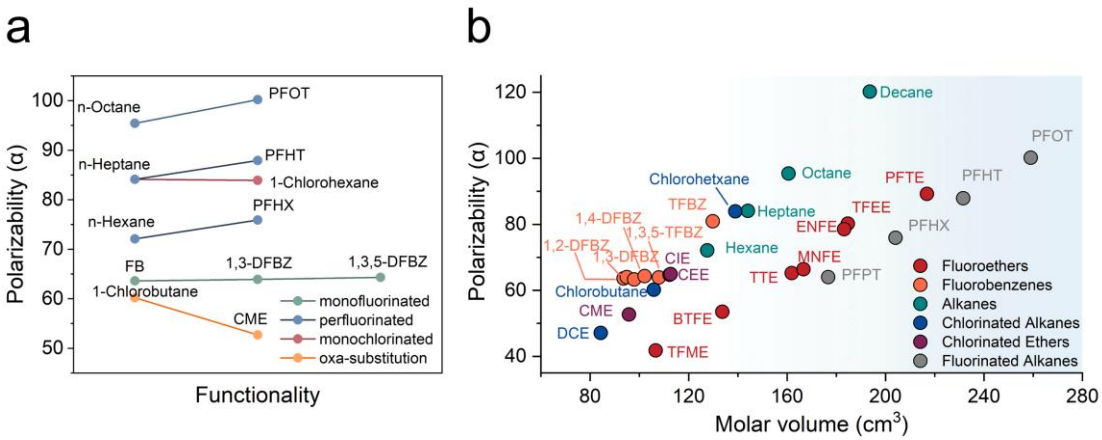

Supplementary Fig. 3 | Influences of (**a**) functional groups and (**b**) molecular volume on polarizability. The x-axis ("Functionality") represents the different functional groups introduced into the molecular framework to illustrate their influence on molecular polarizability.

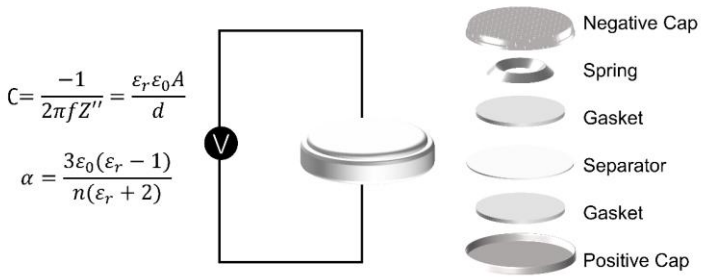

Supplementary Fig. 4 | Structure of the coin cell for polarizability testing.

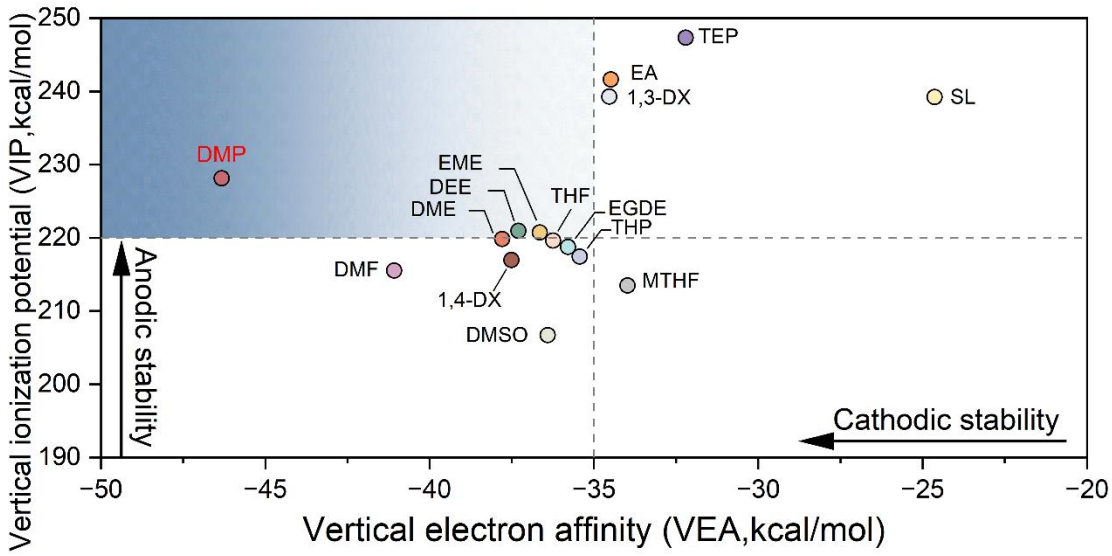

Supplementary Fig. 5 | Diagram of vertical electron affinity versus vertical ionization potential in different solvents.

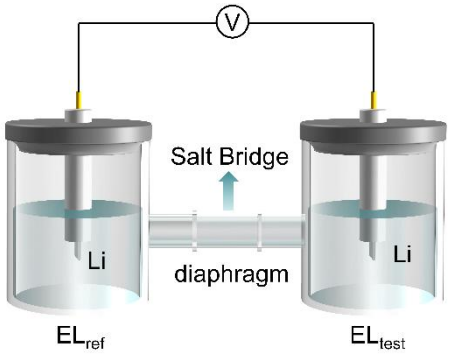

Supplementary Fig. 6 | Schematic diagram of the apparatus for measuring the desolvation energy.

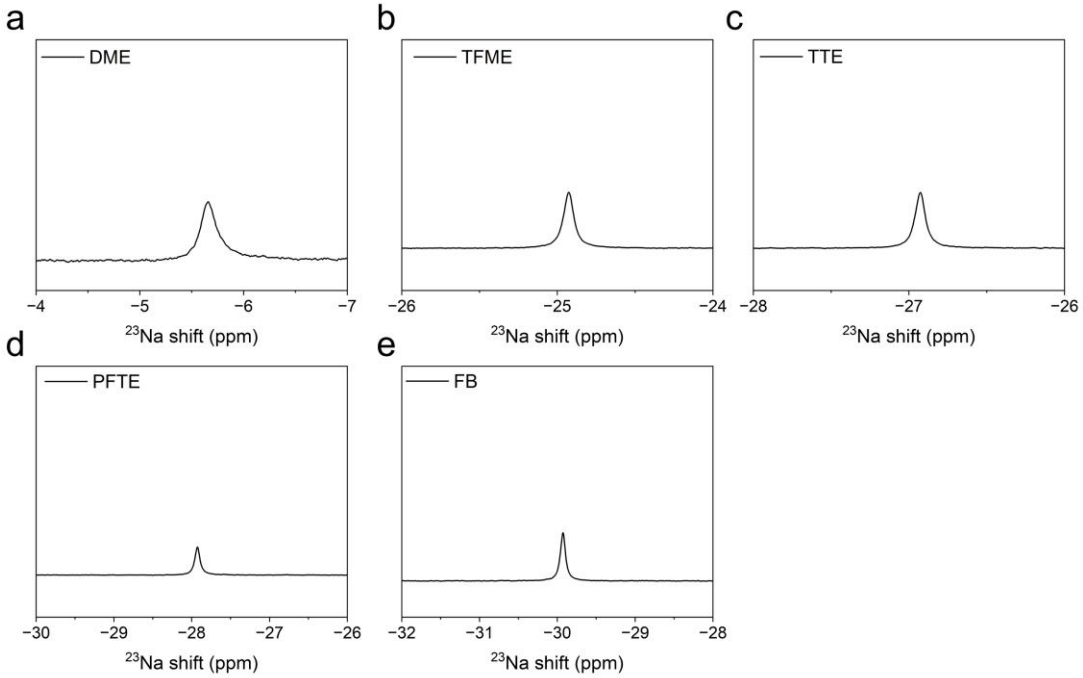

Supplementary Fig. 7 | ^{23}Na NMR spectra of 10 mM NaFSI in (**a**) DME, (**b**) TFME, (**c**) TTE, (**d**) PFTE and (**e**) FB.

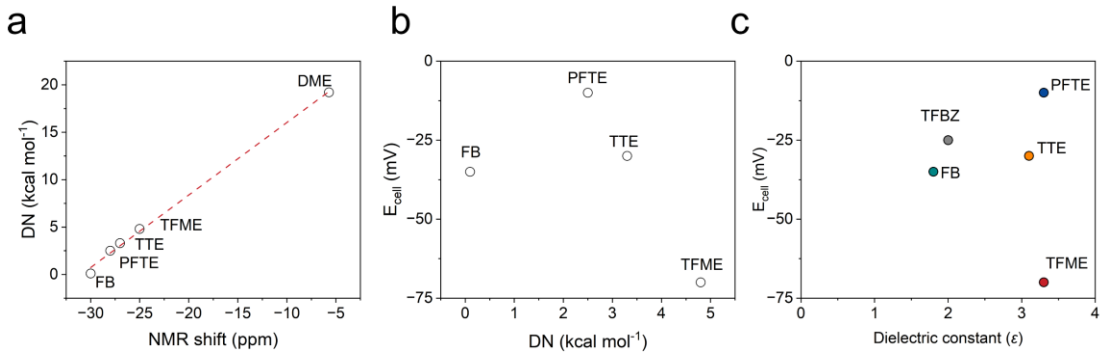

Supplementary Fig. 8 | **a** Plot of the ^{23}Na shift of NaTFSI dissolved in various inert solvents versus their DN. Influences of (**b**) DN and (**c**) dielectric constant on the desolvation energy.

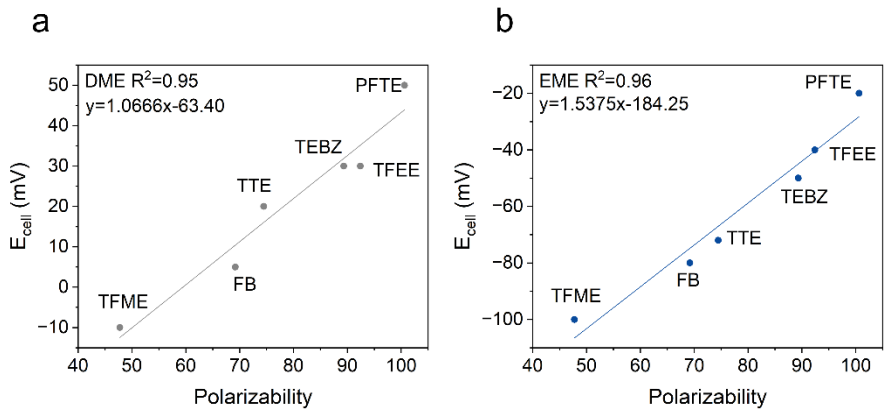

Supplementary Fig. 9 | Linear correlations between polarizability of inert solvents and desolvation energy in (**a**) DME-based electrolytes and (**b**) EME-based electrolytes.

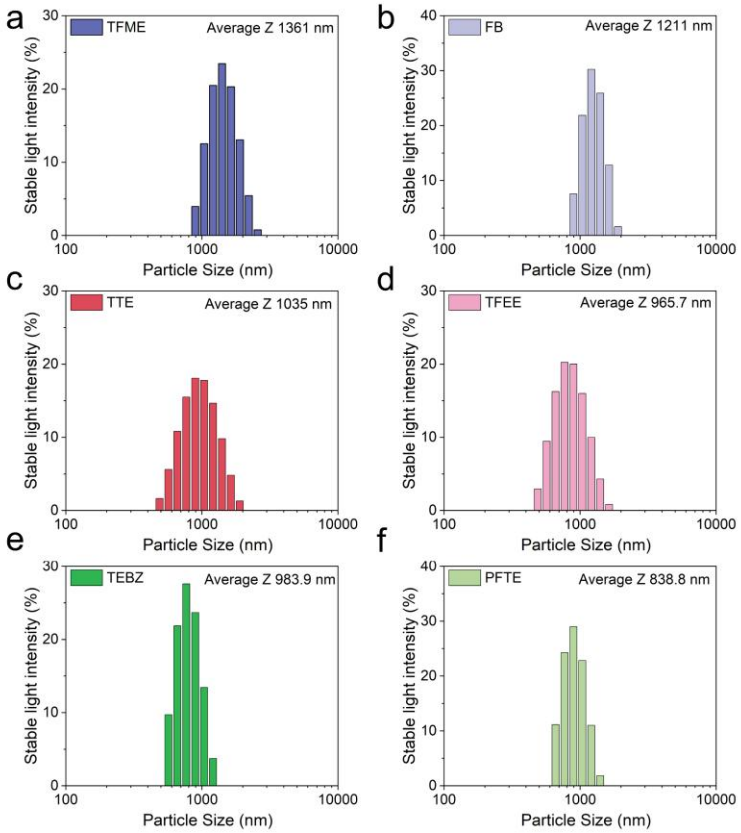

Supplementary Fig. 10 | Average cluster particle size distribution of electrolytes containing six representative inert solvents with different polarizabilities. (**a**) TFME, (**b**) FB, (**c**) TTE, (**d**) TFEE, (**e**) TEBZ, (**f**) PFTE.

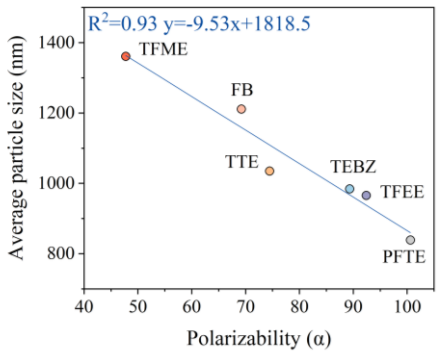

Supplementary Fig. 11 | Linear correlation between the average cluster particle size of electrolytes containing six representative inert solvents and the polarizability of the inert solvents.

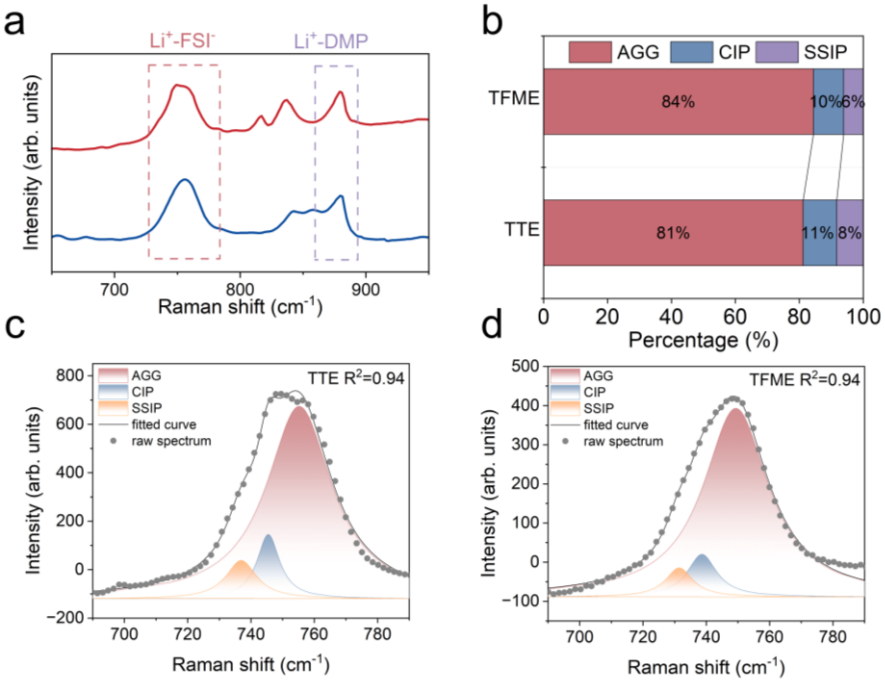

Supplementary Fig. 12 | Raman characterization of TTE and TFME electrolytes. **a** Raman spectra of TTE and TFME electrolytes. **b** Relative proportions of SSIP, CIP and AGG species obtained from Raman peak deconvolution. **c** Peak deconvolution of the Raman spectrum for the TTE electrolyte. **d** Peak deconvolution of the Raman spectrum for the TFME electrolyte.

The static Raman spectra indicate that the solvation structure in both TTE and TFME electrolytes shows no significant difference, with both maintaining a similar solvation structure.

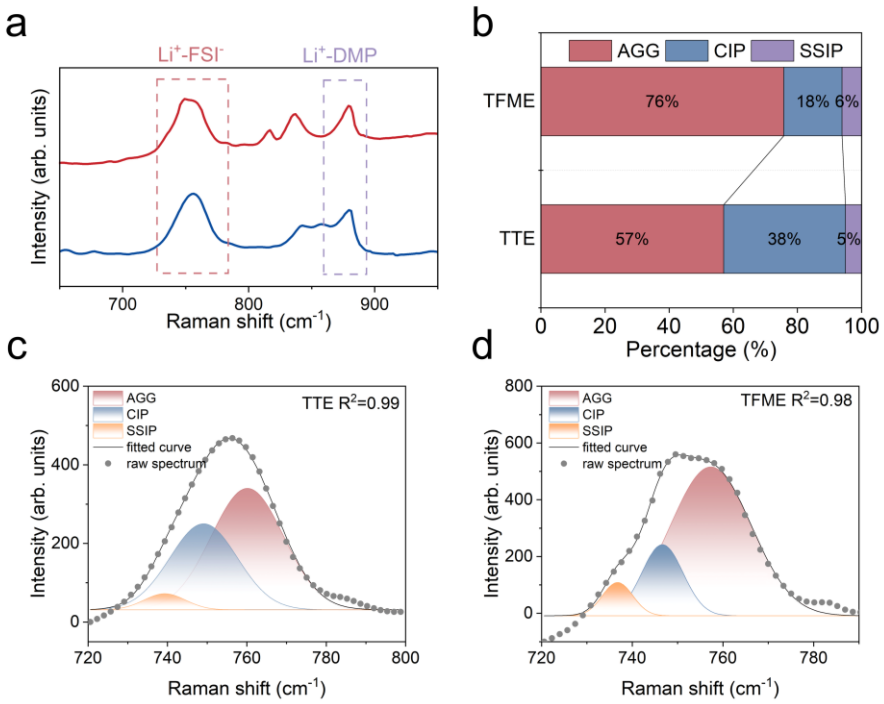

Supplementary Fig. 13 | *In situ* Raman spectra of TTE and TFME electrolytes collected from point 2 of the discharge stage in Fig. 3a. **a** Raman spectrum of the TTE electrolyte. **b** Raman spectrum of the TFME electrolyte. **c** Relative proportions of the solvation structures obtained from Raman analysis for the TTE electrolyte. **d** Relative proportions of the solvation structures obtained from Raman analysis for the TFME electrolyte.

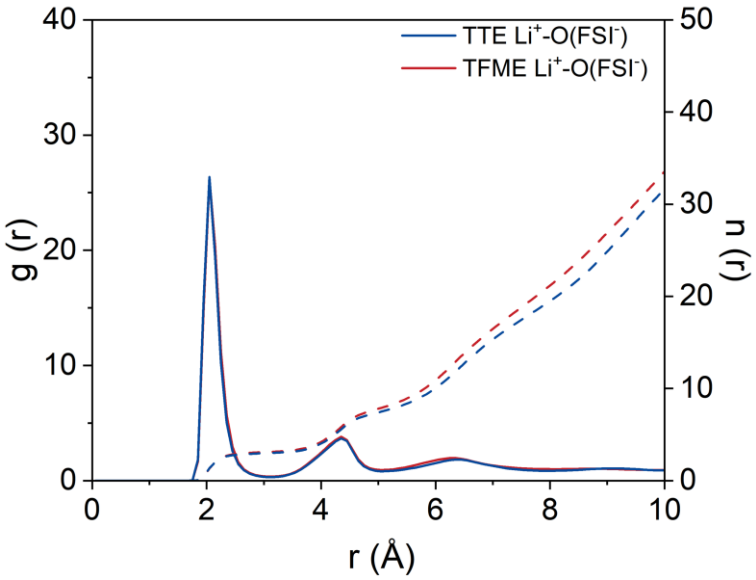

Supplementary Fig. 14 | Radial distribution functions (RDF) calculated from MD simulations of the TTE and TFME electrolytes.

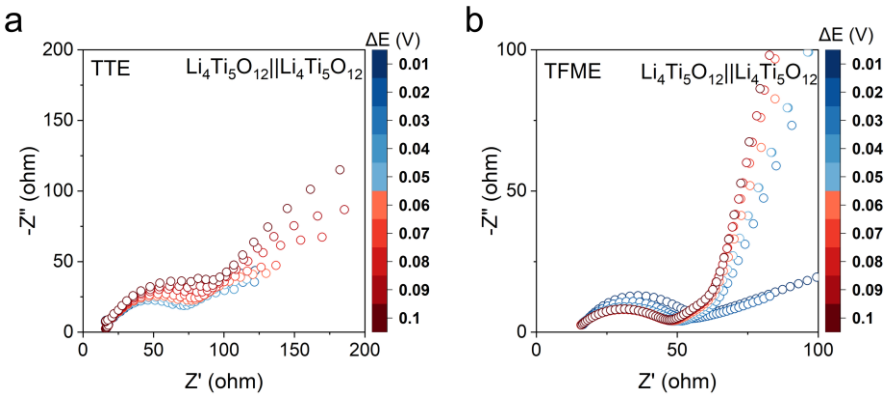

Supplementary Fig. 15 | EIS plots of symmetric $Li_4Ti_5O_{12}||Li_4Ti_5O_{12}$ cells with (**a**) TTE and (**b**) TFME electrolytes.

To identify the interfacial desolvation of Li^+ and avoid the interference of SEI, $Li_4Ti_5O_{12}||Li_4Ti_5O_{12}$ cells were assembled to conduct EIS tests under different bias voltages[9,10]. Prior to this, each $Li_4Ti_5O_{12}$ electrode was discharged to its lithiation platform, ensuring identical potential for both electrodes. All EIS plots in Supplementary Fig. 15 exhibit only one semicircle, which corresponds to the interfacial desolvation of Li^+. The diameter of semicircle increases more inconspicuous in TFME electrolyte with the increasing bias voltage, revealing a more stable Li^+ transport.

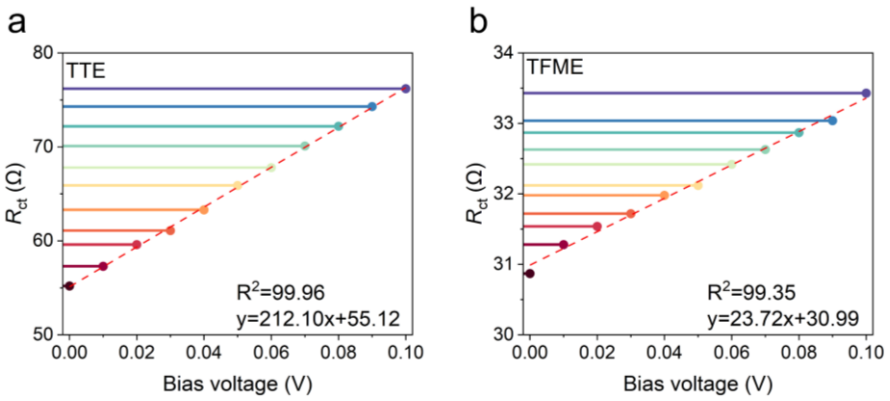

Supplementary Fig. 16 | Fitting plots between R_{ct} and ΔE with (**a**) TTE and (**b**) TFME electrolytes.

The relationship between R_{ct} and ΔE was fitted by a linear function.

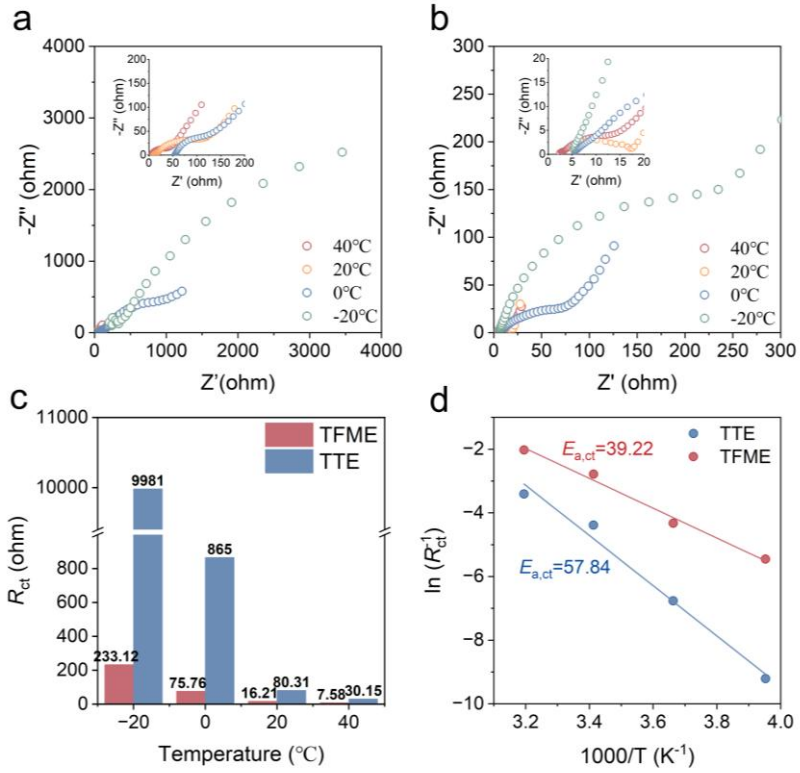

Supplementary Fig. 17 | Nyquist plots of the cycled Li||$Li_4Ti_5O_{12}$ cell with (**a**) TTE and (**b**) TFME electrolytes. The magnified views of the results with the Z′ from (**a**) 0 to 200 Ω in TTE and (**b**) 0 to 20 Ω in TFME are presented in the insets. **c** Summarized results of charge transfer resistances (R_{ct}) and (**d**) activation energies for charge transfer in different electrolytes.

The activation energy was determined following the procedure established in our prior work[11].

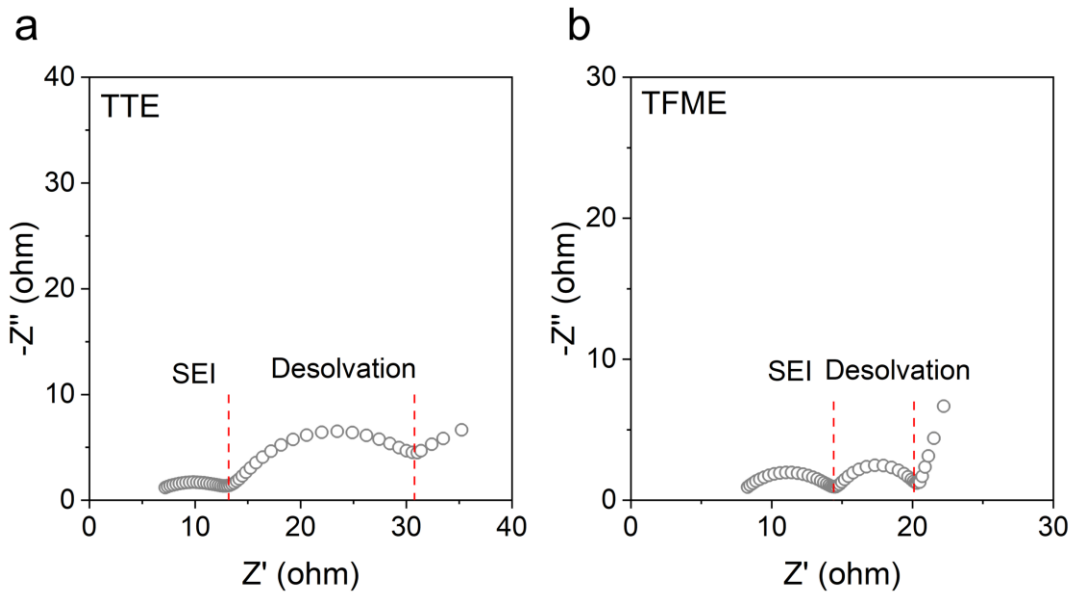

Supplementary Fig. 18 | EIS of Li||Cu cells with (**a**) TTE and (**b**) TFME electrolytes.

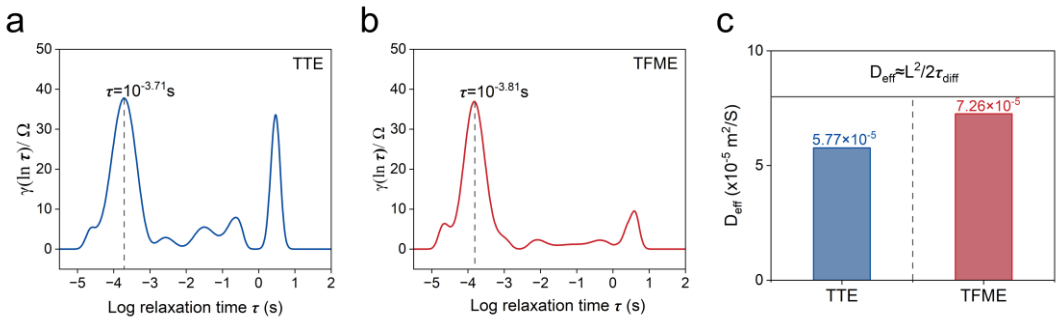

Supplementary Fig. 19 | The DRT plot derived from EIS data in Li||Cu cells with (**a**) TTE and (**b**) TFME electrolytes and (**c**) the corresponding effective migration rate calculated from the DRT method.

The effective migration rate was derived from the DRT method on Li||Cu cells. This analysis demonstrates that the ion migration rate of TFME electrolyte is better than that of TTE electrolyte.

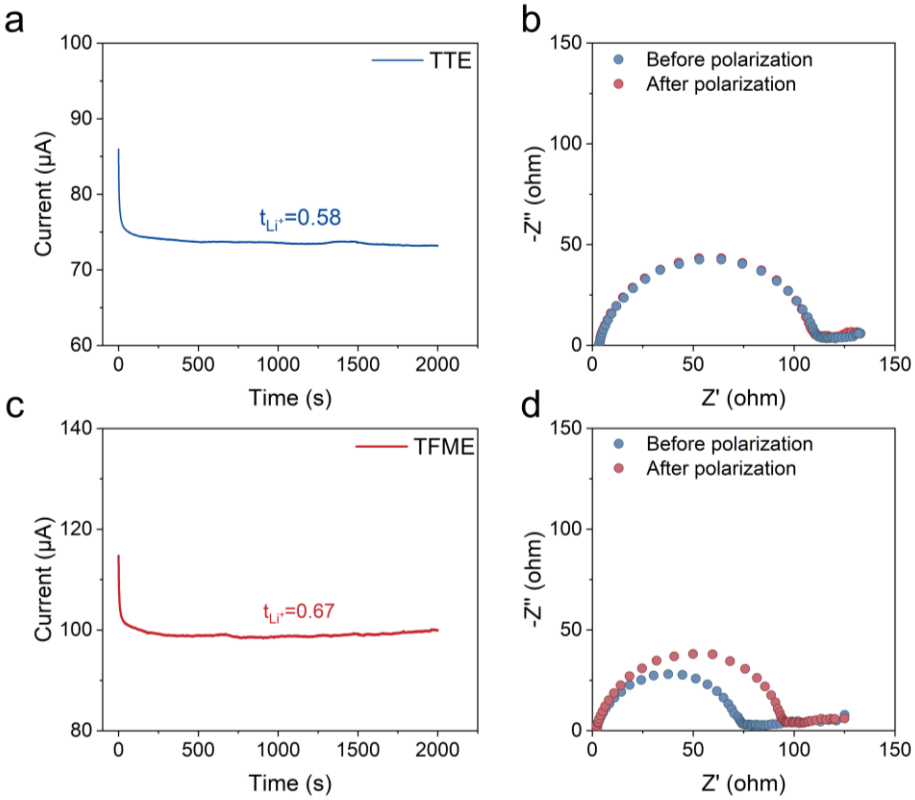

Supplementary Fig. 20 | Li^+ transference number of (**a**, **b**) TTE and (**c**, **d**) TFME electrolytes.

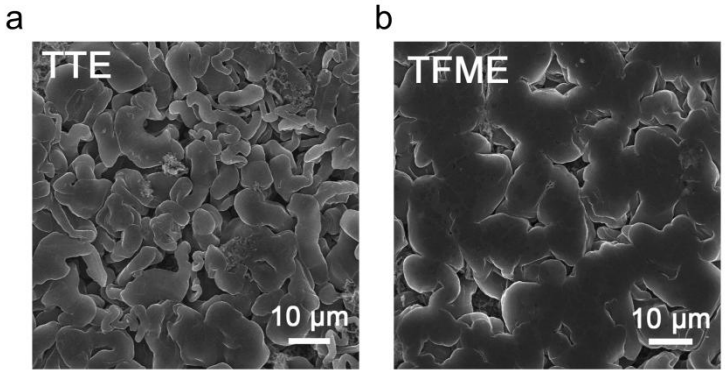

Supplementary Fig. 21 | Top-view SEM images of the Li plating morphologies on Cu substrates in (**a**) TTE and (**b**) TFME electrolytes at a current density of 0.5 mA cm^{-2} and areal capacity of 3 mAh cm^{-2}.

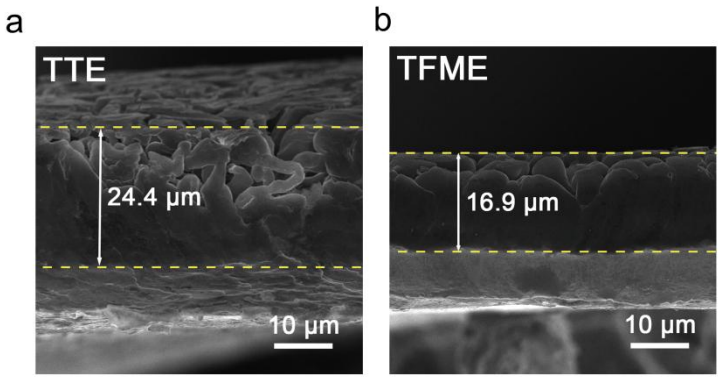

Supplementary Fig. 22 | Cross-section-view SEM images of the Li plating morphologies on Cu substrates in (**a**) TTE and (**b**) TFME electrolytes at a current density of 0.5 mA cm^{-2} and areal capacity of 3 mAh cm^{-2}.

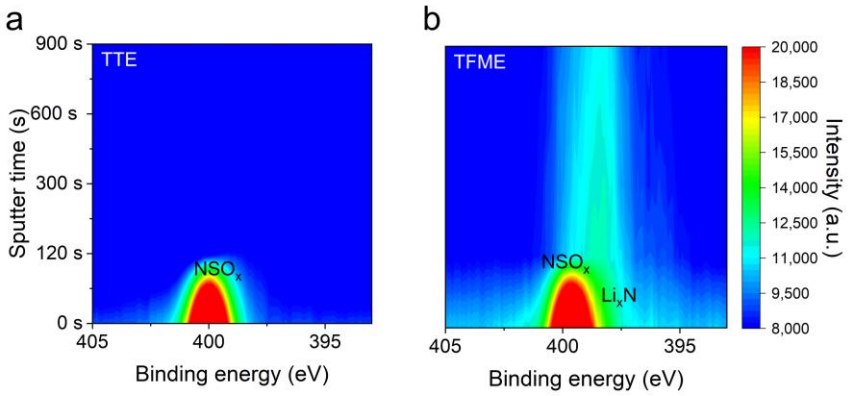

Supplementary Fig. 23 | XPS depth profiles of N 1*s* on Li deposit in (**a**) TTE and (**b**) TFME electrolytes.

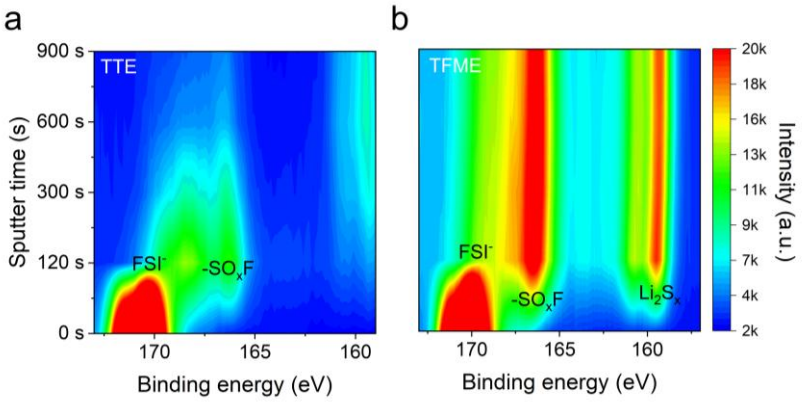

Supplementary Fig. 24 | XPS depth profiles of S 2*p* on Li deposit in (**a**) TTE and (**b**) TFME electrolytes.

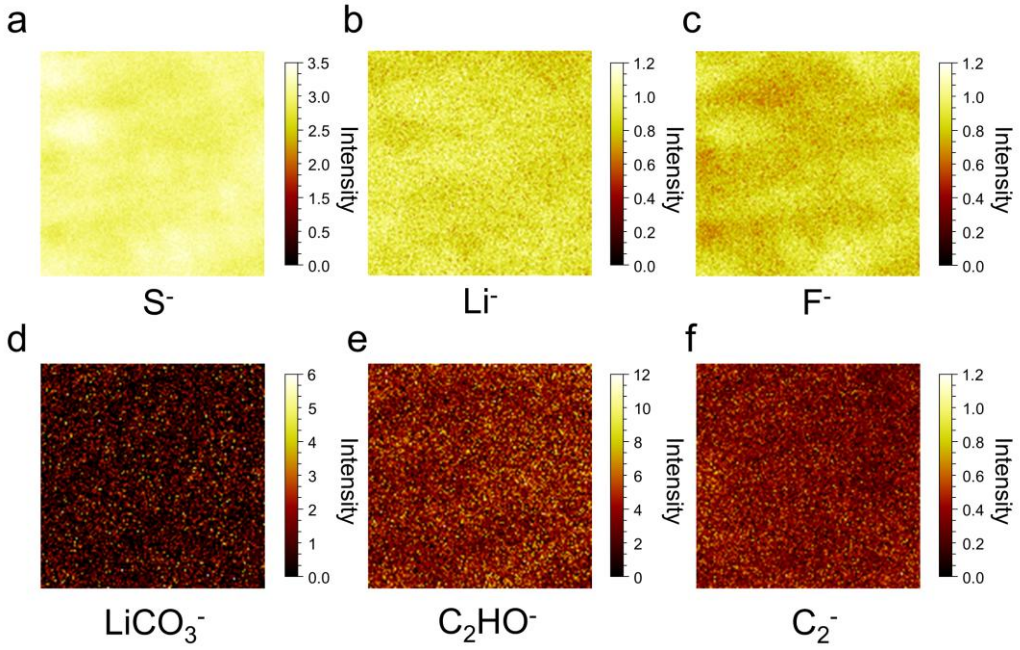

Supplementary Fig. 25 | Fragment mapping for (**a**) S^-, (**b**) Li^-, (**c**) F^-, (**d**) $LiCO_3^-$, (**e**) C_2HO^- and (**f**) C_2^- of Li deposits in TFME electrolyte. The Li deposits were obtained by plating 6 mAh cm^{-2} of Li onto Cu foil at 0.5 mA cm^{-2} and 25 °C prior to sample collection.

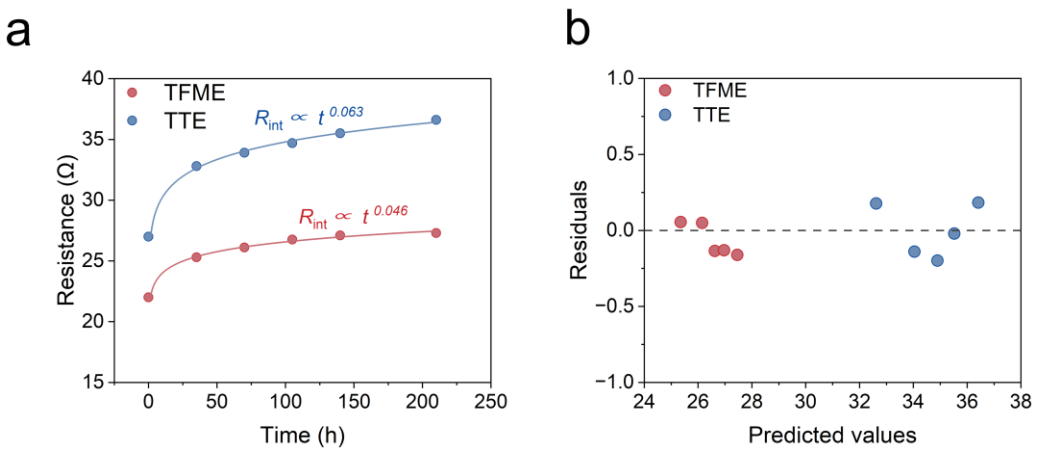

Supplementary Fig. 26 | Time-dependent changes of interfacial resistance (R_{int}). **a** Non-linear fitting of R_{int} and t (h) based on a power law. **b** Residual plot showing the difference between observed and predicted values.

R_{int} is a time-dependent factor that characterizes the calendar aging of lithium metal negative electrode in electrolytes. An empirical law was employed to fit the temporal evolution of R_{int}. In Supplementary Fig. 26a, the exponents describe the aging rate of lithium metal negative electrode in TTE (0.063) and TFME (0.046) electrolytes. Moreover, the residual plot illustrates the deviation of the data to the power-law model, further confirming the rapid passivation of lithium metal negative electrode in TFME electrolyte[12-14].

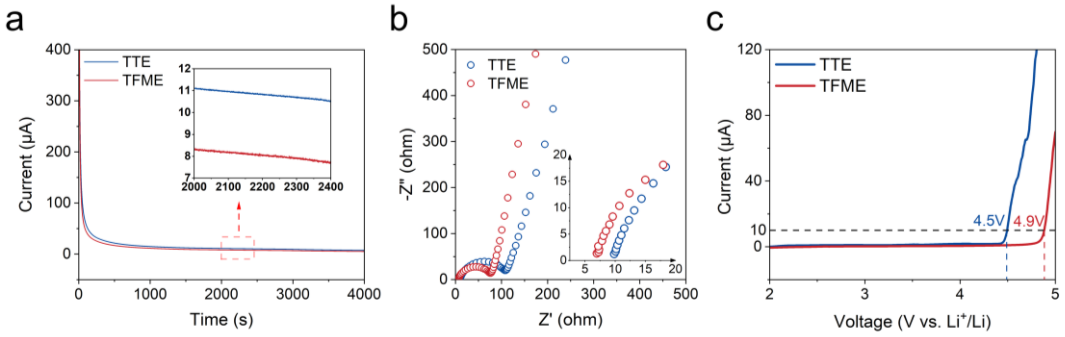

Supplementary Fig. 27 | Comparison of cathodic and anodic stability of TTE and TFME electrolytes. **a** Chronoamperometry measurement of Li||Cu cells at 0.1 V voltage stage. The inset shows the magnified results from 2000 to 2400 seconds. **b** EIS plots of Li||Cu cells after the chronoamperometry tests. The inset shows the magnified results with the Z′ from 0 to 20 Ω in two electrolytes. **c** LSV plots of Li||Al cells within the voltage window of 3–6 V (0.5 mV s^{-1}).

The protective effect of integrated Li^+ solvates-derived SEI on inhibiting the electrolyte decomposition by lithium metal negative electrode was investigated by chronoamperometry test at 0.1 V. The relative stability of TTE and TFME electrolytes to lithium metal negative electrode can be empirically evaluated by observing the differences in current density[15]. As shown in Supplementary Fig. 27a, the chronoamperometry result reveals elevated current densities that derive from TTE electrolyte degradation. This result indicates that the SEI generated in TTE electrolyte exhibits weaker protective effect against the electrolyte decomposition by lithium metal negative electrode compared to the TFME electrolyte. The accelerated decomposition leads to the accumulation of interfacial impedance in TTE electrolyte (Supplementary

Fig. 27b). Furthermore, Supplementary Fig. 27c highlights the better anodic stability of the TFME electrolyte compared to the TTE electrolyte.

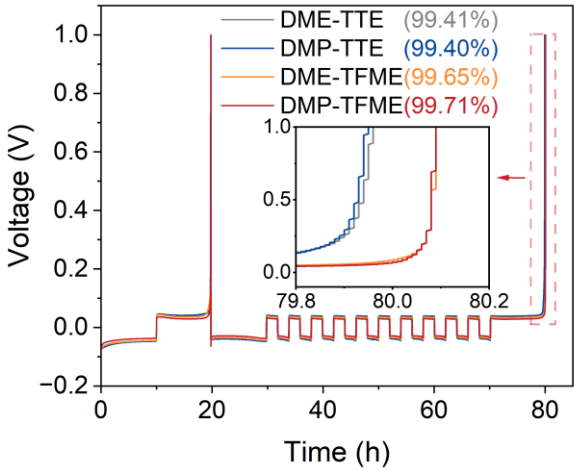

Supplementary Fig. 28 | Lithium metal CEs in Li||Cu cells by the modified Aurbach's method at 25℃. The inset provides an enlarged view of the Coulombic efficiency, highlighting the difference between the two electrolytes.

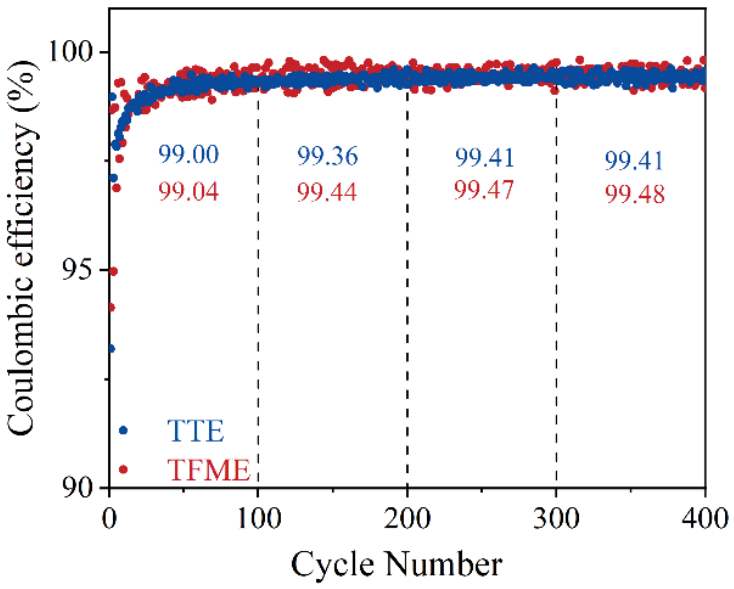

Supplementary Fig. 29 | Cycle performance of Li||Cu cells with TTE and TFME electrolytes at 25 °C. Charge/discharge cycles were tested at 0.5 mA cm^{-2} with a fixed capacity of 1 mAh cm^{-2}.

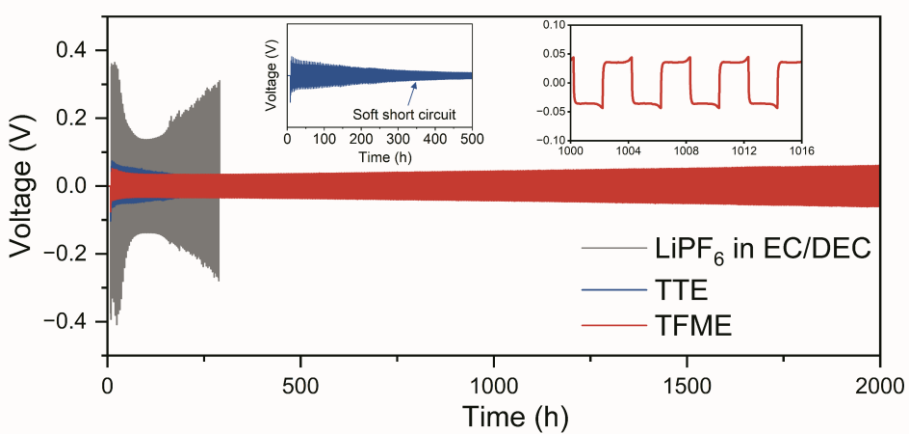

Supplementary Fig. 30 | Cycle performance of Li||Li cells at 25 ℃ (0.5 mA cm^{-2}/1 mAh cm^{-2}). The inset plots show the soft short circuit in TTE electrolyte at around 450th cycle (left) and normal cycling from 1000th and 1016th cycles in TFME electrolyte (right).

Li||Li cells were employed to evaluate the effects of inert solvents with different polarizabilities on interfacial stability during Li plating/stripping. As shown in Supplementary Fig. 30, Li||Li cells with TFME electrolytes exhibit longer lifespan and smaller polarization than cells with commercial carbonate electrolyte. Moreover, TFME enables a stable Li plating/stripping cycle of over 2000 h with smaller voltage hysteresis (~36 mV) than TTE (~68 mV). A premature short-circuit after 400 h is observed in TTE electrolyte.

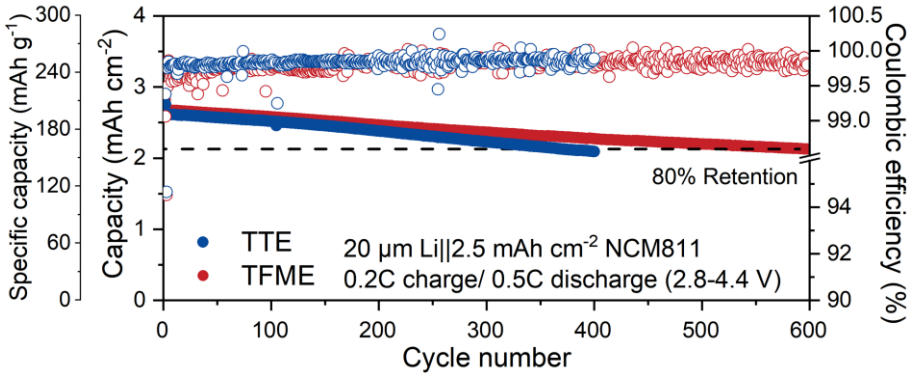

Supplementary Fig. 31 | Cycle performance of Li||NCM811 cells at 25 °C (0.2C charge/0.5C discharge, 1C = 200 mA g^{-1} based on the NCM811 positive electrode, N/P ratio: 1.6).

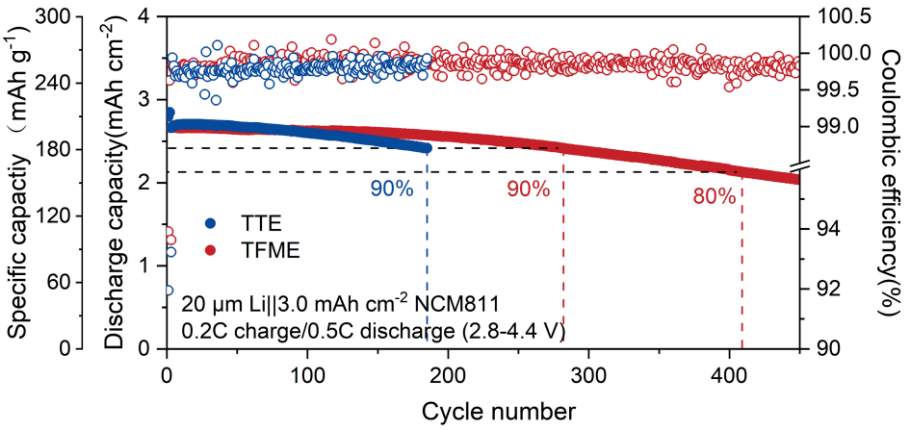

Supplementary Fig. 32 | Cycle performance of Li||NCM811 cells at 25 ℃ (0.2C charge/0.5C discharge, 1C = 200 mA g^{-1} based on the NCM811 positive electrode, N/P ratio: 1.3).

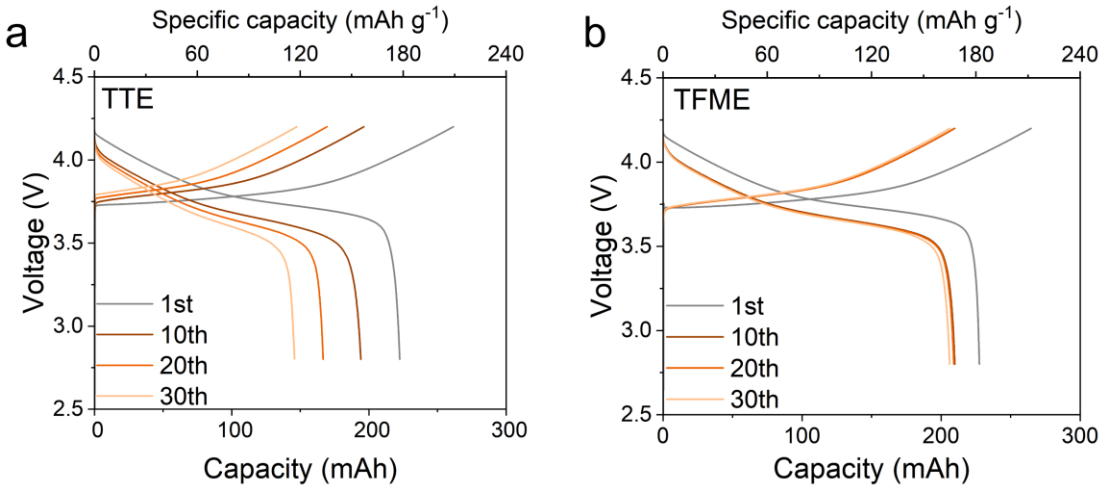

Supplementary Fig. 33 | Charge/discharge curves of the multiple cycles (1^{st}, 10^{th}, 20^{th}, 30^{th}) in (**a**) TTE electrolyte and (**b**) TFME electrolyte.

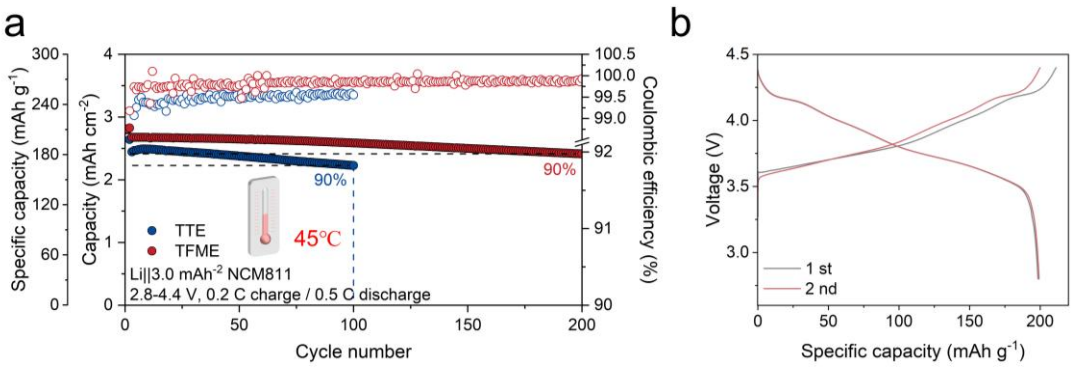

Supplementary Fig. 34 | (**a**) Cycle performance of Li||NCM811 cells employing an excess lithium metal negative electrode at 45 °C (0.2C charge/0.5C discharge, 1C = 200 mA g^{-1} based on the NCM811 positive electrode). (**b**) Voltage profiles of the first two formation cycles collected at 25 ± 1 °C and 0.1 C prior to the high-temperature electrochemical evaluation.

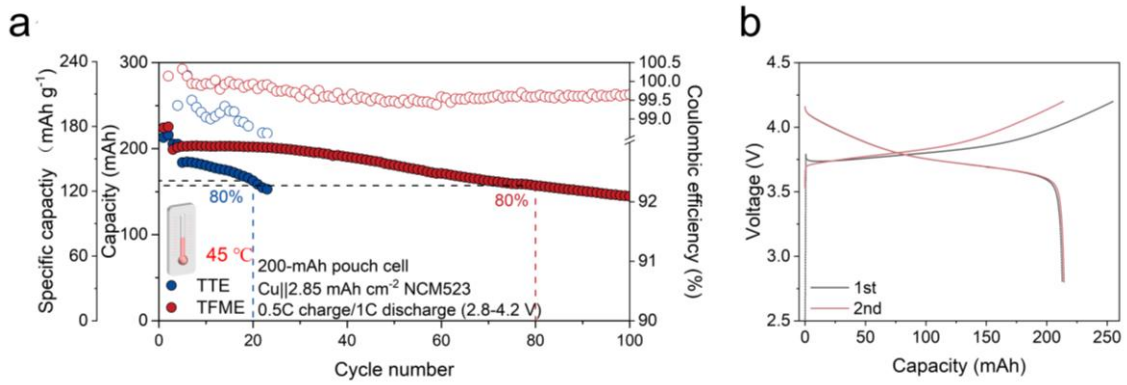

Supplementary Fig. 35 | (**a**) Cycle performance of 200-mAh Cu||NCM523 pouch cells at 45 °C (1C = 160 mA g^{-1} based on the NCM523 positive electrode, N/P ratio: 0). (**b**) Voltage profiles of the first two activation (formation) cycles collected at 25 ± 1 °C and 0.1 C prior to the high-temperature electrochemical evaluation.

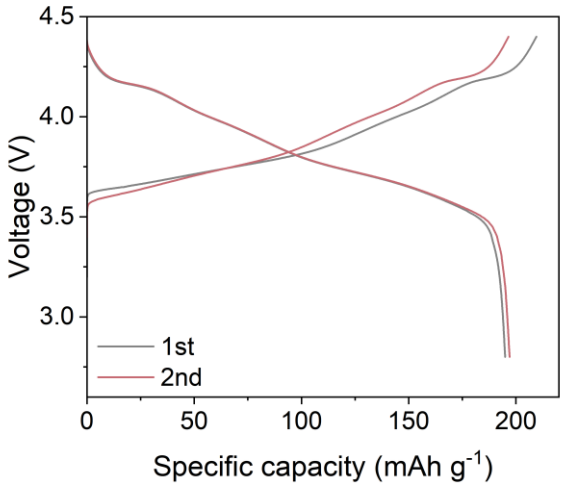

Supplementary Fig. 36 | Voltage profiles of the first two formation cycles of Li||NCM811 cells employing an excess lithium metal negative electrode.

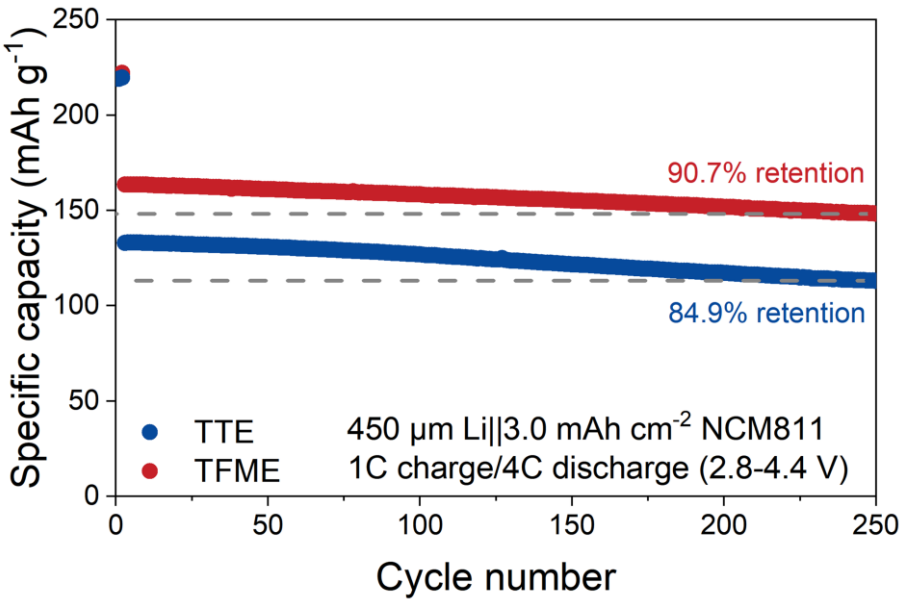

Supplementary Fig. 37 | Cycle performance of Li||NCM811 cells employing an excess lithium metal negative electrode cycled at 25 °C (1C charge/4C discharge, 1C = 200 mA g^{-1} based on the NCM811 positive electrode).

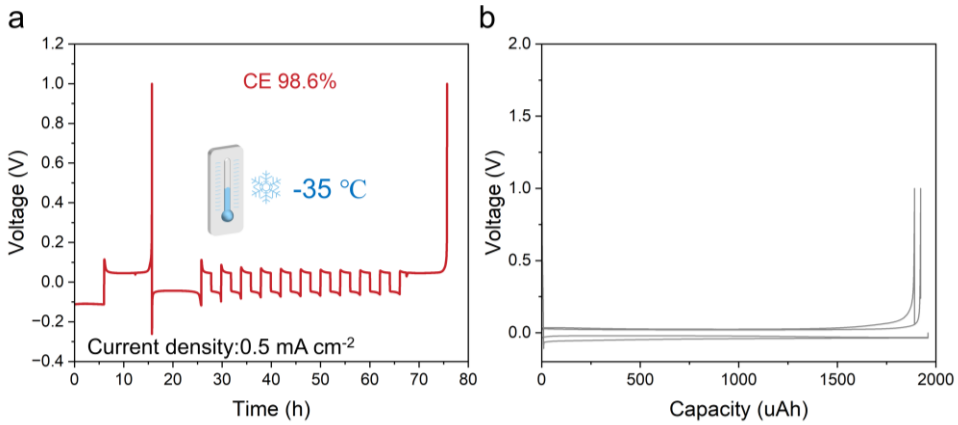

Supplementary Fig. 38 | (a) Li metal CE in Li||Cu cell by the modified Aurbach's method at a low temperature of −35℃. (**b**) Voltage profiles of the activation cycles conducted at 25 ± 1 °C with a plating/stripping capacity of 1.0 mAh cm^{-2} at 0.5 mA cm^{-2} prior to the low-temperature CE measurements.

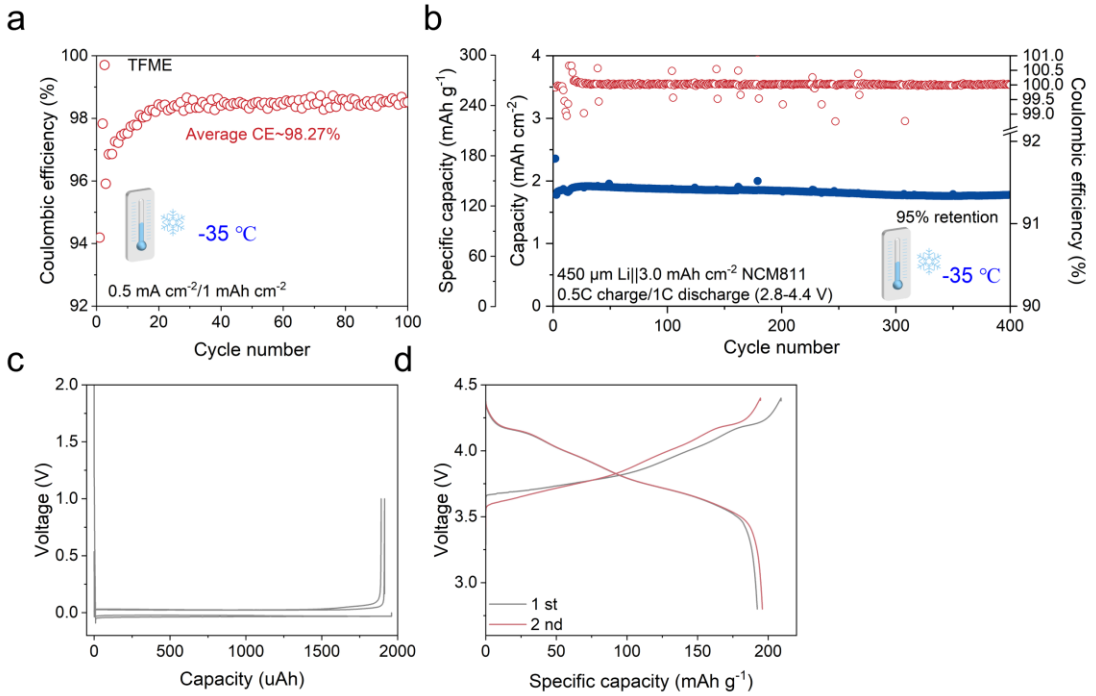

Supplementary Fig. 39 | Cycle performance of (**a**) Li||Cu half cell at −35 °C and (**b**) Li||NCM811 cell employing an excess lithium metal negative electrode at a charge rate of 0.5C and a discharge rate of 1C at −35 °C (1C = 200 mA g^{-1} based on the NCM811 positive electrode). (**c**) Voltage profiles of the activation cycles conducted at 25 ± 1 °C with a plating/stripping capacity of 1.0 mAh cm^{-2} at 0.5 mA cm^{-2} prior to the low-temperature Li||Cu measurements. (**d**) Voltage profiles of the first two formation cycles collected at 25 ± 1 °C and 0.1 C prior to the low-temperature cycling test of Li||NCM811 cells.

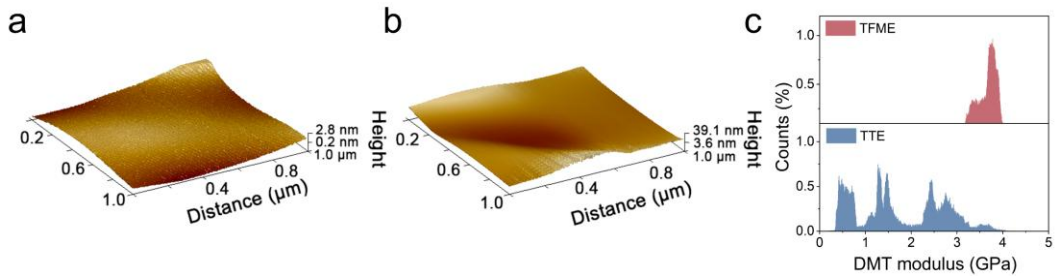

Supplementary Fig. 40 | The height image of the SEI formed in (**a**) TFME and (**b**) TTE electrolytes.

c DMT modulus distribution of the SEI formed in two electrolytes.

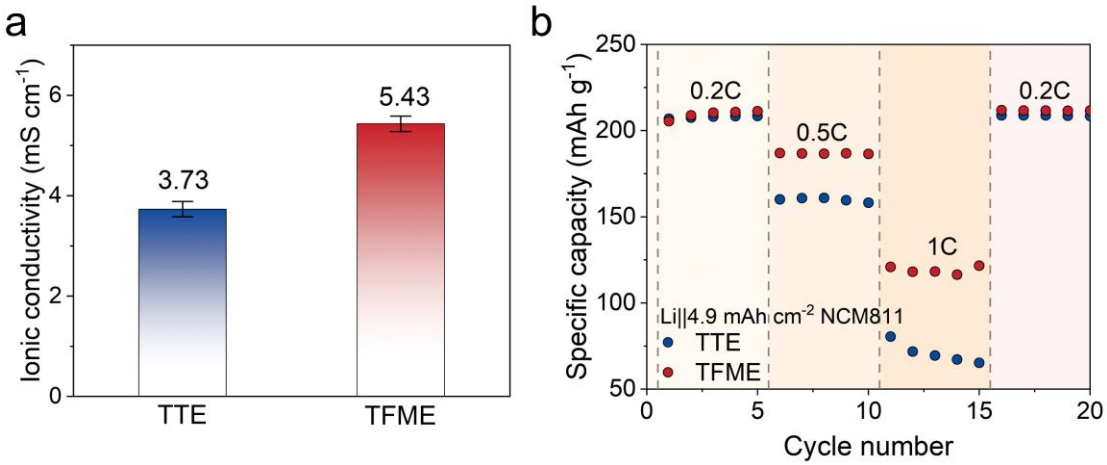

Supplementary Fig. 41 | **a** Ionic conductivities of TTE and TFME electrolytes. Each sample was measured three times and the average value was taken. **b** Rate capability of Li||4.9 mAh cm^{-2} NCM811 cells employing an excess lithium metal negative electrode with TTE and TFME electrolytes at 25 ℃ (1C = 200 mA g^{-1} based on the NCM811 positive electrode).

Supplementary Fig. 42 | Quality measurement of a 7.5-Ah lithium metal pouch cell with TFME electrolyte.

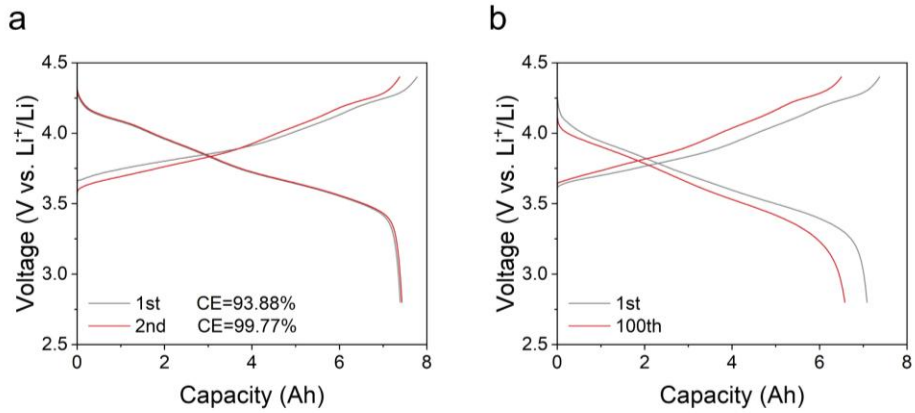

Supplementary Fig. 43 | a Formation cycles of 7.5 Ah-lithium metal pouch cell with TFME electrolyte (0.1C charge/discharge within 2.8–4.4 V). **b** Charge/discharge profiles of 7.5 Ah-lithium metal pouch cell with TFME electrolyte (0.15C charge/0.3C discharge within 2.8–4.4 V, 1C = 200 mA g^{-1} based on the NCM811 positive electrode).

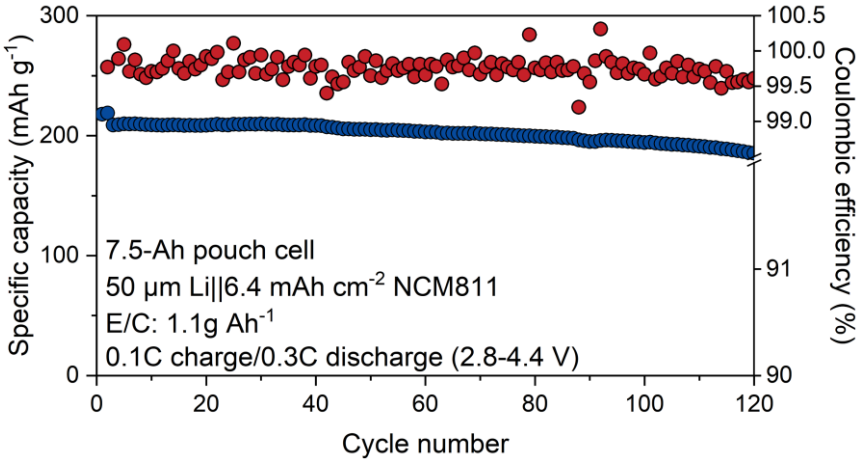

Supplementary Fig. 44 | Cycle performance of 7.5-Ah Li||NCM811 pouch cell using specific capacity as the left Y-axis (0.1C charge/0.3C discharge, 1C = 200 mA g^{-1} based on the NCM811 positive electrode).

Supplementary Table 1. Polarizabilities of the inert solvents.

Name	SMILES No.	Measured Polarizability (10^{-40} $C^2/N \cdot m$)	Theoretical Polarizability (10^{-40} $C^2/N \cdot m$)
TTE	C(F)(F)C(F)(F)COC(F)(F)C(F)F	66.8	65.2
TFBZ	FC(F)(F)OC1=CC=CC=C1	79.2	80.9
TFME	COC(F)(F)C(F)F	38.2	41.8
TFEE	C(OC(F)(F)C(F)F)COC(F)(F)C(F)F	76.3	80.2
PFTE	C(F)(F)C(F)(F)C(F)(F)C(F)(F)COC(F)(F)C(F)F	85.5	89.2
FB	FC1=CC=CC=C1	61.2	63.6
BTFE	O(CC(F)(F)F)CC(F)(F)F	49.7	53.5
MNFE	C(F)(F)(F)C(F)(F)C(F)(F)C(F)(F)OC	64.9	66.4
ENFE	C(F)(F)(F)C(C(OCC)(F)F)(F)C(F)(F)F	76.5	78.5
1,2-DFBZ	FC1=C(F)C=CC=C1	61.2	64.0
1,3-DFBZ	FC1=CC(F)=CC=C1	60.2	63.9
1,4-DFBZ	FC1=CC=C(F)C=C1	60.9	63.7

1,3,5-TFBZ	FC1=CC(F)=CC(F)=C1	64.1	64.3
n-Hexane	CCCCCC	69.4	72.1
n-Heptane	CCCCCCC	80.5	84.1
n-Octane	CCCCCCCC	91.2	95.4
Decane	CCCCCCCCCC	113.6	120.2
DCE	ClCCCl	44.7	47.1
1-Chlorobutane	CCCCCl	57.3	60.2
1-Chlorohexane	CCCCCCl	81.2	83.9
CME	COCCCl	49.9	52.7
CEE	CCOCCCl	63.3	64.7
CIE	CC(C)OCCl	65.1	64.9
PFPT	FC(F)(F)C(F)(F)C(F)(F)C(F)(F)C(F)(F)F	60.3	64.0
PFHX	FC(F)(F)C(F)(F)C(F)(F)C(F)(F)C(F)(F)C(F)(F)F	70.5	75.9

PFHT	FC(F)(F)C(F)(F)C(F)(F)C(F)(F)C(F)(F)C(F)(F)C(F)(F)F	87.2	87.9
PFOT	FC(F)(F)C(F)(F)C(F)(F)C(F)(F)C(F)(F)C(F)(F)C(F)(F)F	96.4	100.2

Supplementary Table 2. The specific distribution of the clusters shown in Figure 3j.

TTE without E		**TTE with E**		**TFME without E**		**TFME with E**	
Cluster Size	Cluster number	Cluster Size	Cluster number	Cluster Size	Cluster number	Cluster Size	Cluster number
99	1	20	2	109	1	31	1
72	1	19	3	67	1	29	1
60	1	11	4	59	1	20	3
50	1	10	29	58	1	19	1
41	1	9	57	41	1	11	6
40	1	1	56	31	2	10	24
39	2			30	3	9	56
31	1			29	2	1	51
30	2			22	1		
29	3			20	2		
21	1			19	4		
20	2			11	3		
19	3			10	10		
11	2			9	18		
10	7			1	23		
9	17						
1	19						

Supplementary Table 3. Summary of literature reports used for comparison in Fig. 5b, including cell configuration, testing conditions, and electrochemical performance of initially anode-free pouch cells.

Ref.	Cell chemistry	N/P ratio	Temperature (℃)	Positive eletrode mass loading (mA cm^{-2})	Electrolyte-to-capacity ratio (g Ah^{-1})	Performance
Ref.4	Cu‖NCM523	0	25	2.85	3	80% capacity retention at 100 cycles
Ref.19	Cu‖NCM523	0	25	3.1	2.4	70% capacity retention at 100 cycles
Ref.20	Cu‖NCM523	0	25	3	2	68% capacity retention at 100 cycles
Ref.25	Cu‖NCM811	0	25	4.2	3	80% capacity retention at 70 cycles

Ref.41	Cu||NCM811	0	25	4.5	3	73% capacity retention at 65 cycles
Ref.42	Cu||NCM811	0	25	4.25	3	76% capacity retention at 100 cycles
Ref.43	Cu||NCM811	0	25	2.75	/	50% capacity retention at 30 cycles
Ref.44	Cu||LFP	0	25	1.6	/	60% capacity retention at 50 cycles
Ref.45	Cu||NCM523	0	25	2.85	3	82% capacity retention at 100 cycles
Ref.46	Cu||LFP	0	25	/	/	40% capacity retention at 100 cycles
Ref.47	Cu||NCM111	0	25	2	/	40% capacity retention at 50 cycles

Ref.48	Cu||NCM111	0	25	2.4	2	80% capacity retention at 90 cycles
Ref.49	Cu||LMNO	0	25	1.83	/	50% capacity retention at 50 cycles
This work	Cu||NCM523	0	25	2.85	3	80% capacity retention at 114 cycles 70% capacity retention at 143 cycles

Supplementary Table 4. Detailed parameters of the 7.5-Ah lithium metal pouch cell

Cell component	Specification	Parameters
Positive electrode (NCMS85E)	Number	13
	Active material mass loading (mg cm^{-2}, each side)	29.13
	Specific areal capacity (mAh cm^{-2}, each side)	6.4
	The Weight of Al foil（g）	1.63
	The Weight of Al foil + NCM (g)	37.16
Negative electrode Li	Number	14
	Thickness (μm)	100 (50 μm for each side)
	Weight (g)	3.95
Electrolyte	electrolyte/capacity (g/Ah)	1.10
	Weight (g)	7.44
Separator	Weight (g)	0.97
package and lugs	Weight (g)	2.0
	Dimension (cm × cm)	7 × 11
Full cell	Discharge capacity (Ah)	7.5
	Discharge energy (Wh)	27.885
	Total weight (g)	51.49
	Specific energy (Wh kg^{-1})	541.56
Pressure	Stacking pressure (Mpa)	0.729

References

1. Francesca Terenziani, A. P. Static polarizability of molecular materials. *J. Chem. Phys.* **118**, 10617-10624 (2003).
2. Frederick, J. Strains and polarization developed during electric field application on dielectric materials. *J. Mater. Sci.* **45**, 123-134 (2010).
3. HunterWoodward, W. H. Broadband dielectric spectroscopy—a practical guide. *Pure Appl. Chem.* **80**, 1239-1251 (2008).
4. Florina Branzoi, V. B., Zoia Pahom. Modified electrodes obtained by electrochemical codeposition of some conducting polymers on metallic substrate. *Rev. Roum. Chim.* **61**, 1007-1014 (2016).
5. Talebian, E. and Talebian, M. A general review on the derivation of Clausius–Mossotti relation. *Optik* **124**, 2324-2326 (2013).
6. Lu, S. et al. First-principles-based optimized design of fluoride electrolytes for sodium-ion batteries. *Molecules* **27**, 6949 (2022).
7. Fadel, E. R. et al. Role of solvent-anion charge transfer in oxidative degradation of battery electrolytes. *Nat. Commun.* **10**, 3360 (2019).
8. Kim, S. C. et al. Potentiometric measurement to probe solvation energy and its correlation to lithium battery cyclability. *J. Am. Chem. Soc.* **143**, 10301-10308 (2021).
9. Zhang, S. et al. Oscillatory solvation chemistry for a 500 Wh kg^{-1} Li-metal pouch cell. *Nat. Energy* **9**, 1285-1296 (2024).
10. Xu, K. et al. Differentiating contributions to "ion transfer" barrier from interphasial resistance and Li^+ desolvation at electrolyte/graphite interface. *Langmuir* **26**, 11538-

11543 (2010).

11. Sun, C. et al. 50C Fast-charge Li-ion batteries using a graphite anode. *Adv. Mater.* **34**, e2206020 (2022).

12. Boyle, D. T. et al. Corrosion of lithium metal anodes during calendar ageing and its microscopic origins. *Nat. Energy* **6**, 487-494 (2021).

13. Kwon, H. et al. Borate–pyran lean electrolyte-based Li-metal batteries with minimal Li corrosion. *Nat. Energy* **9**, 57-69 (2023).

14. Attia, P. M. et al. Revisiting the $t^{0.5}$ dependence of SEI growth. *J. Electrochem. Soc.* **167**, 090535 (2020).

15. Zhao, Q. et al. On the crystallography and reversibility of lithium electrodeposits at ultrahigh capacity. *Nat. Commun.* **12**, 6034 (2021).